

# Characterization and Performance of Germanium Detectors with sub-keV Sensitivities for Neutrino and Dark Matter Experiments

A.K. Soma,<sup>1,2,\*</sup> M.K. Singh,<sup>1,2,†</sup> L. Singh,<sup>1,2,‡</sup> G. Kiran Kumar,<sup>1,§</sup> F.K. Lin,<sup>1</sup> Q. Du,<sup>3</sup> H. Jiang,<sup>4</sup> S.K. Liu,<sup>3,4</sup> J.L. Ma,<sup>4</sup> V. Sharma,<sup>1,2</sup> L. Wang,<sup>4</sup> Y.C. Wu,<sup>4</sup> L.T. Yang,<sup>4</sup> W. Zhao,<sup>4</sup> M. Agartioğlu,<sup>1,5</sup> G. Asryan,<sup>1</sup> Y.Y. Chang,<sup>1</sup> J.H. Chen,<sup>1</sup> Y.C. Chuang,<sup>1</sup> M. Deniz,<sup>1,5,6</sup> C.L. Hsu,<sup>1</sup> Y.H. Hsu,<sup>1</sup> T.R. Huang,<sup>1</sup> L.P. Jia,<sup>4</sup> S. Kerman,<sup>1,5</sup> H.B. Li,<sup>1</sup> J. Li,<sup>4</sup> F.T. Liao,<sup>1</sup> H.Y. Liao,<sup>1</sup> C.W. Lin,<sup>1</sup> S.T. Lin,<sup>1,3</sup> V. Marian,<sup>7</sup> X.C. Ruan,<sup>8</sup> B. Sevda,<sup>1,5</sup> Y.T. Shen,<sup>1</sup> M.K. Singh,<sup>1,2</sup> V. Singh,<sup>2</sup> A. Sonay,<sup>1,5</sup> J. Su,<sup>4</sup> V.S. Subrahmanyam,<sup>1,2</sup> C.H. Tseng,<sup>1</sup> J.J. Wang,<sup>1</sup> H.T. Wong,<sup>1,¶</sup> Y. Xu,<sup>1,9</sup> S.W. Yang,<sup>1</sup> C.X. Yu,<sup>1,9</sup> Q. Yue,<sup>4</sup> and M. Zeyrek<sup>6</sup>

(TEXONO Collaboration)

<sup>1</sup> *Institute of Physics, Academia Sinica, Taipei 11529, Taiwan.*

<sup>2</sup> *Department of Physics, Institute of Science, Banaras Hindu University, Varanasi 221005, India.*

<sup>3</sup> *Department of Physics, Sichuan University, Chengdu 610065, China.*

<sup>4</sup> *Department of Engineering Physics, Tsinghua University, Beijing 100084, China.*

<sup>5</sup> *Department of Physics, Dokuz Eylül University, Buca, İzmir 35160, Turkey.*

<sup>6</sup> *Department of Physics, Middle East Technical University, Ankara 06531, Turkey.*

<sup>7</sup> *CANBERRA-Lingolsheim Facility, Lingolsheim 67380, France.*

<sup>8</sup> *Department of Nuclear Physics, Institute of Atomic Energy, Beijing 102413, China.*

<sup>9</sup> *Department of Physics, Nankai University, Tianjin 300071, China.*

(Dated: September 2, 2016)

Germanium ionization detectors with sensitivities as low as 100 eV<sub>ee</sub> (electron-equivalent energy) open new windows for studies on neutrino and dark matter physics. The relevant physics subjects are summarized. The detectors have to measure physics signals whose amplitude is comparable to that of pedestal electronic noise. To fully exploit this new detector technique, various experimental issues including quenching factors, energy reconstruction and calibration, signal triggering and selection as well as evaluation of their associated efficiencies have to be attended. The efforts and results of a research program to address these challenges are presented.

PACS numbers: 29.40.-n, 14.60.Lm, 95.35.+d.

## I. INTRODUCTION

Sensitivities on several important research programs in neutrino and dark matter physics can be significantly enhanced when the “physics threshold” can be lowered to extend the dynamic range of signal detection [1, 2]. This motivates efforts to characterize detector behavior and to devise analysis methods in domains where the amplitude of physics signals is comparable to that caused by fluctuations of pedestal electronic noise.

In this article, we report on our research program and results on using advanced germanium (Ge) ionization detectors to address the above mentioned issues. Following a survey on physics topics relevant to low-background and low-threshold techniques, crucial aspects of detector operation and optimizations near electronic “noise-edge” are discussed. These include studies on energy estimators and calibration, trigger and data acquisition rates,

signal event selections and evaluation of their efficiencies.

Data taken with point-contact Ge detectors with sub-keV sensitivities were adopted to establish the results. However, the devised techniques would also be applicable to other detector systems, and at other energy ranges. Unless otherwise stated, electron-equivalent energy (eV<sub>ee</sub>) is used throughout this article to denote detector response to a measurable energy  $T$ . The raw kinetic energy due to nuclear recoils is denoted by keV<sub>nr</sub>.

Results on the characterization and performance of Ge detectors are original work. Surface background [3] and quenching factor [4] of Ge detectors have been discussed in the literature. They are summarized in Sections IV C 2 and III D, respectively, for completeness and coherence.

## II. SCIENTIFIC MOTIVATIONS

The objective of our research program is to develop detectors with modular mass of  $\mathcal{O}(1 \text{ kg})$ , physics threshold of  $\mathcal{O}(100 \text{ eV}_{ee})$  and background level at threshold of  $\mathcal{O}(1 \text{ kg}^{-1} \text{ keV}_{ee}^{-1} \text{ day}^{-1})$  [1]. Germanium semiconductors in ionization mode were selected as the detection technique. When these “benchmark” specifications are fulfilled, several important topics discussed in subsequent sections can be experimentally pursued.

\*Present Address: Department of Physics, University of South Dakota, Vermillion, South Dakota 57069, USA.

†Corresponding Author: manoj@gate.sinica.edu.tw

‡Corresponding Author: lakhwinder@gate.sinica.edu.tw

§Present Address: Physics Department, KL University, Guntur 522502, India.

¶Corresponding Author: ht Wong@phys.sinica.edu.tw

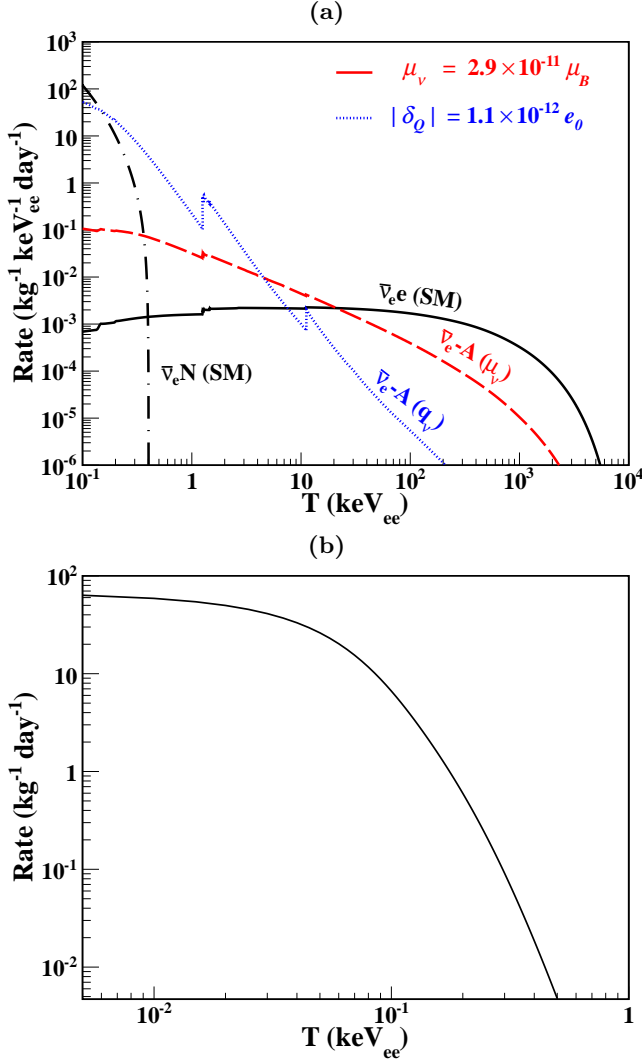


FIG. 1: (a) Observable spectra due to reactor- $\bar{\nu}_e$  interactions on Ge target with  $\phi(\bar{\nu}_e) = 10^{13} \text{ cm}^{-2}\text{s}^{-1}$ , neutrino magnetic moment and neutrino milli-charge fraction at the current bounds from direct experimental searches:  $\mu_\nu = 2.9 \times 10^{-11} \mu_B$  and  $|\delta_Q| = 1.1 \times 10^{-12}$ , respectively. Superimposed are SM  $\bar{\nu}_e$ -e and coherent scattering  $\bar{\nu}_e$ -N. Quenching effects of nuclear recoils are taken into account. (b) Expected integral  $\bar{\nu}_e$ -N coherent scattering rates due to SM contributions at the same flux, as a function of physics threshold, assuming realistic detector resolution.

### A. Neutrino Electromagnetic Properties

Investigations of neutrino properties and interactions can reveal physics within and beyond the Standard Model (SM). An avenue is the study of possible neutrino electromagnetic interactions [5].

The neutrino magnetic moment ( $\mu_\nu$ ) is an intrinsic neutrino property that describes possible neutrino-photon couplings via its spin [6, 7]. The helicity is flipped in these  $\mu_\nu$ -induced interactions. Observations of  $\mu_\nu$  at levels relevant to present or future generations of exper-

iments would strongly favor the case of Majorana neutrinos [8]. Most experimental searches of  $\mu_\nu$  make use of neutrino interactions with free electrons. The differential cross-section has an  $(1/T)$ -dependence, where the measurable  $T$  is due to recoil kinetic energy of electrons. The expected differential spectra for reactor neutrinos at a flux of  $\phi(\bar{\nu}_e) = 10^{13} \text{ cm}^{-2}\text{s}^{-1}$  are shown in Figure 1a (details of reactor  $\bar{\nu}_e$ -spectra and their derivations are described in Refs. [7, 9]). Contributions from  $\mu_\nu$  are enhanced as  $T$  decreases, with necessary modifications from the atomic binding energy effects [10, 11].

In a similar spirit, studies on neutrino “milli-charge” probe possible helicity conserving QED-like interactions. It can be parametrized as  $(\delta_Q \cdot e_0)$  where  $\delta_Q$  is the charge fraction and  $e_0$  is the standard electron charge. Finiteness of  $\delta_Q$  would imply that neutrinos are Dirac particles. An enhancement in cross-sections induced by atomic effects, as depicted in Figure 1a, has recently been identified [11, 12]. The known ratios of peaks at discrete binding energies provide smoking-gun signatures for positive observations.

It follows from Figure 1a that experimental studies on  $\mu_\nu$  and  $q_\nu$  should focus on  $T < 10 \text{ keV}_{ee}$ . At benchmark experimental sensitivities and with comparable exposure as the GEMMA experiment [13], the potential reaches are  $\mu_\nu \sim 2 \times 10^{-11} \mu_B$  and  $\delta_Q \sim 6 \times 10^{-14}$ , where  $\mu_B$  is the Bohr magneton.

In addition, it was recognized [14] that the  $\mu_\nu$ -induced interaction with matter would have a pronounced enhancement in cross-section, manifesting as measurable peaks when the initial-state neutrinos are non-relativistic. The experimental signatures require good-resolution and low-threshold measurements for which Ge detectors would be optimal.

### B. Neutrino Nucleus Coherent Scattering

The elastic scattering between a neutrino and a nucleus ( $\nu N$ ) [1, 15]

$$\nu + N \rightarrow \nu + N \quad (1)$$

is a fundamental SM interaction that has never been observed [16]. It probes coherence effects in electroweak interactions [17], and provides a sensitive test for physics beyond SM. The coherent interaction plays an important role in astrophysical processes and constitutes the irreducible background to the forthcoming generation of dark matter experiments. Coherent neutrino scattering may provide new approaches to the detection of supernova neutrinos and offer a promising avenue towards a compact and transportable neutrino detector capable of real-time monitoring of nuclear reactors.

The maximum nuclear recoil energy for a Ge target ( $A=72.6$ ) due to reactor  $\bar{\nu}_e$  is about  $2 \text{ keV}_{nr}$ . The quenching factor (QF, discussed in Section III D), is about 0.2 for Ge in the  $< 10 \text{ keV}_{nr}$  region. Accordingly, the maximum measurable energy for nuclear recoil events in Ge

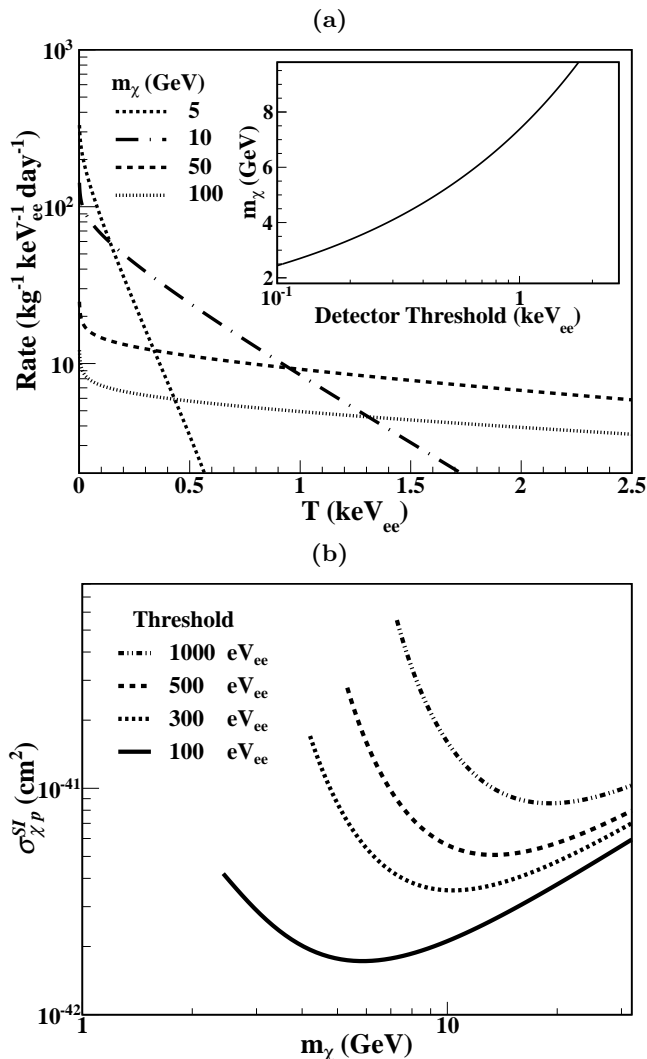


FIG. 2: (a) Recoil spectra for  $\chi$ -Ge interactions at a cross-section of  $10^{-40} \text{ cm}^2$ , at various  $m_\chi$  values. The lower bounds of  $m_\chi$  as a function of physics threshold are shown in the inset, assuming 1 kg-yr of data and a background level of  $1 \text{ kg}^{-1} \text{ keV}_{ee}^{-1} \text{ day}^{-1}$ . Quenching effects of nuclear recoils are taken into account. (b) Sensitivity reach in  $\chi$ -proton spin-independent cross-section ( $\sigma_{\chi p}^{SI}$ ) of the same configuration at different detector thresholds, showing the relative improvement in cross-section as a function of  $m_\chi$ .

due to reactor  $\bar{\nu}_e$  is about 300  $\text{eV}_{ee}$ . The typical differential spectrum and the integral event rate as a function of detection threshold are given in Figures 1a&b, respectively. At benchmark sensitivities, the expected rate is of  $\mathcal{O}(10 \text{ kg}^{-1} \text{ day}^{-1})$  with a signal-to-background ratio  $>50$ . Improvement of the lower reach of detector sensitivity is therefore crucial for such experiments.

### C. Dark Matter Searches

Weakly Interacting Mass Particles (WIMPs, denoted by  $\chi$ ) are leading dark matter candidates [18]. The elastic scattering between WIMPs and the nuclei

$$\chi + N \rightarrow \chi + N \quad (2)$$

is the favored channel in direct dark matter search experiments. Consistency with observations on formation of cosmological structures requires that WIMPs should be massive and non-relativistic. In addition, interactions between WIMPs and matter may be both spin-independent and spin-dependent. Requirements of experimental studies on WIMPs are similar to those on neutrino-nucleus coherent scattering, in which a low detector threshold plays a crucial role.

As illustrations, the nuclear recoil spectra for Ge with  $\sigma = 10^{-40} \text{ cm}^2$  at various WIMP masses ( $m_\chi$ ) are displayed in Figure 2a. A reduction in detector threshold opens a new observation window for low-mass WIMPs. A germanium detector with 100  $\text{eV}_{ee}$  threshold would allow light WIMPs with  $m_\chi$  down to 2  $\text{GeV}$  to be probed [19–24]. The sensitivity reach on  $m_\chi$  with 1 kg-yr of exposure as a function of threshold at a background of  $1 \text{ kg}^{-1} \text{ keV}_{ee}^{-1} \text{ day}^{-1}$  is illustrated in the inset of Figure 2a. Moreover, a lower threshold allows a wider range of WIMPs to contribute in an observable interaction and hence results in better sensitivities for all values of  $m_\chi$ , as shown in Figure 2b.

## III. SUB-KEV GERMANIUM DETECTOR

### A. Detector and Readout

Data taken with four Ge detectors are adopted in this study. The detectors and their characteristics are listed as follows, while their respective sensor electrode schematics are depicted in Figures 3a,b,c&d.

1. Conventional coaxial p-type high purity Ge detector (CoaxGe) with 1 kg in mass, used as target detector in Ref. [7];
2. 4-element array of n-type Ge detector with 5 g modular mass, a pilot “ultra-low-energy” germanium detector (ULEGe) used in Refs. [19, 22];
3. p-type point-contact Ge detector (pPCGe) with 500 g mass, similar in functionalities but not in detector mass to those used as target detectors in Refs. [20, 23]; and
4. n-type point-contact Ge detector (nPCGe) with 500 g mass, used as calibration detector in Refs. [3, 20].

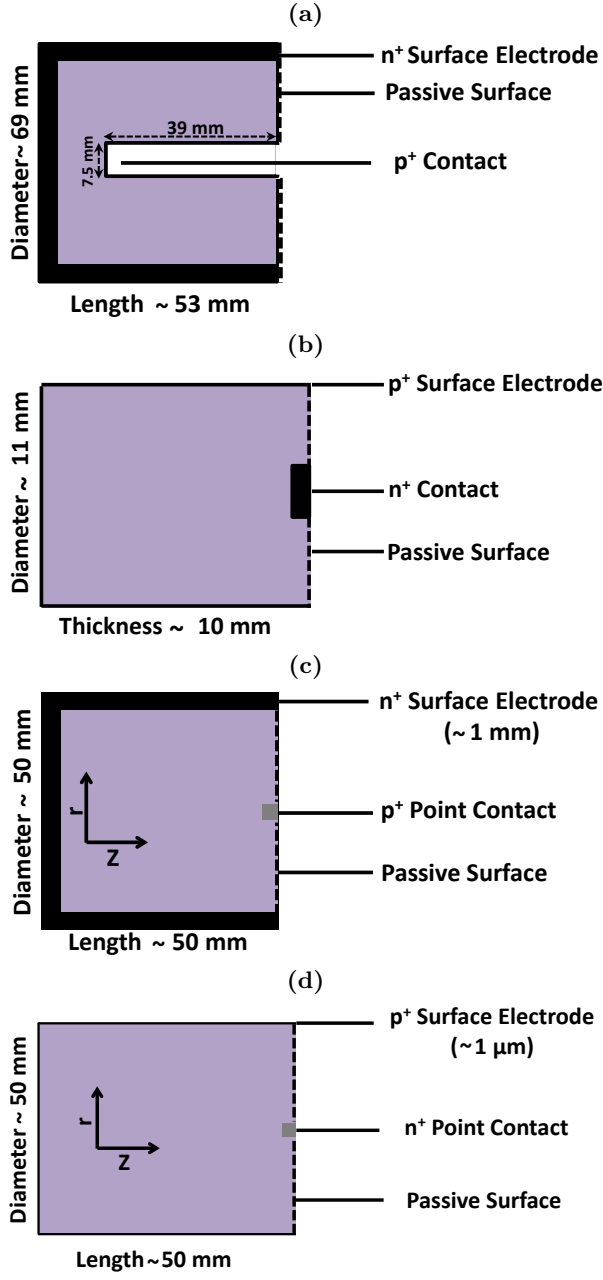


FIG. 3: Schematic crystal configuration of Ge detectors discussed in this article: (a) CoaxGe with 1 kg mass, (b) ULEGe with 5 g modular mass, (c) pPCGe with 500 g mass, and (d) nPCGe with 500 g mass.

All the detectors have been procured commercially. CoaxGe and ULEGe are conventional “catalog-item” detectors<sup>1</sup> serving for control and comparison purposes. Both pPCGe and nPCGe are custom-designed and fabricated<sup>2</sup>, and are the primary focuses of this work.

<sup>1</sup> Canberra Meriden, USA.

<sup>2</sup> Canberra Lingolsheim, France.

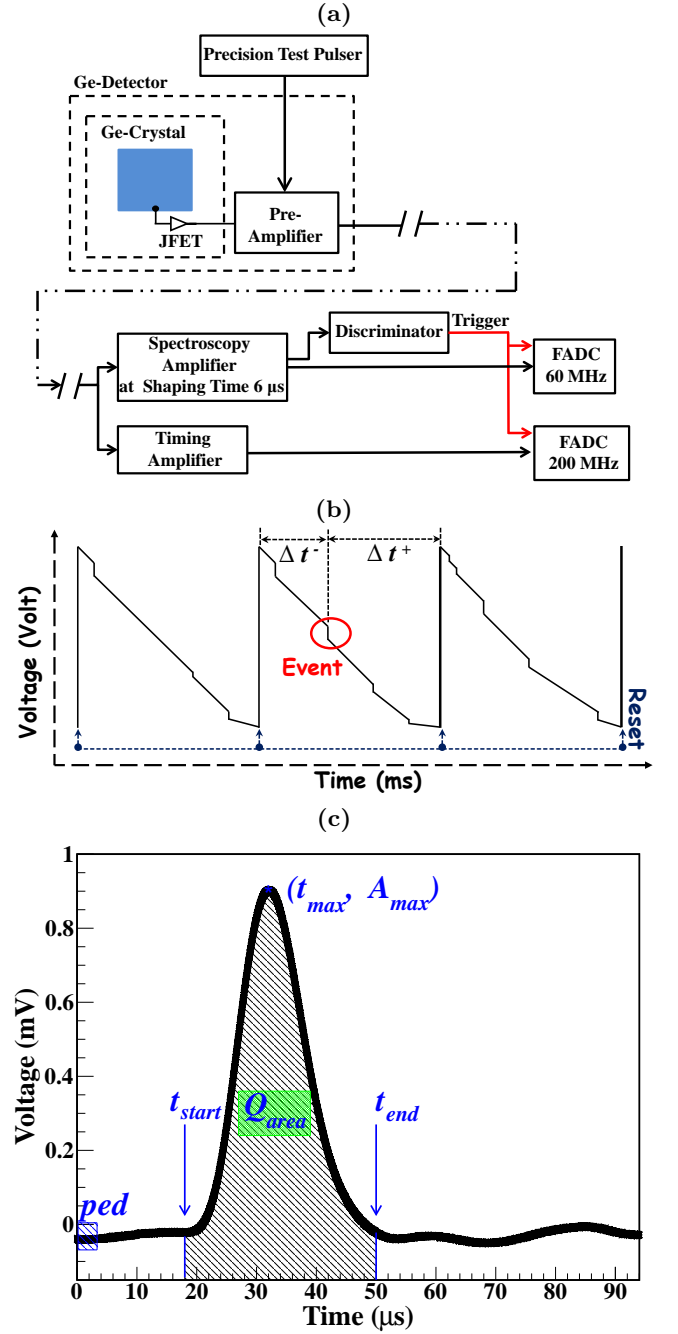


FIG. 4: (a) Schematic diagram of the DAQ system for detector performance characterization reported in this work. The system in the experiment at KSNL includes readout of NaI(Tl) anti-Compton detector and cosmic-ray veto scintillator panels. (b) Schematic drawing of raw preamplifier signals as recorded with an oscilloscope. The RESET amplitude and time interval of different detectors are summarized in Table I. (c) Typical SA<sub>6</sub> pulse at 6 μs shaping time. Various key parameters for analysis and calibration purposes are shown in both (b) and (c).

The concept of point-contact Ge detectors was proposed and the first nPCGe with 800 g mass was constructed in the 1980s [25], followed by recent realization of pPCGe [2] for low-threshold, low-background experiments. Sub-keV threshold is realized using ULEGe, pPCGe and nPCGe through optimizing the detector configurations that reduces the output capacitance to  $\sim$ pF, and through improving the front-end “JFET” electronics. The subsequent discussions apply to these three detectors, except those on differentiation of surface and bulk events in Section IV C 2i, which are relevant only to pPCGe. The performance parameters of the four detectors in this study are summarized in Table I, while those of earlier benchmark projects with Ge detectors in which threshold is crucial are listed in Table II for comparison.

A schematic diagram of the readout scheme for characterizing Ge detectors is illustrated in Figure 4a. Signals from Ge-crystal sensors are first amplified by front-end JFETs<sup>3</sup> located in the vicinity of the Ge diodes. Outputs are fed to reset preamplifiers<sup>4</sup> placed  $\sim$ 30 cm away. The typical output as observed on an oscilloscope is displayed in Figure 4b. The saw-tooth waveform exemplifies the timing structures of “RESETs” issued after a fixed time interval or when charge deposition in the detector exceeds a pre-set value (for example, with a direct cosmic-ray event). The steps in between RESETs represent physics signals whose energy is proportional to the step size.

As depicted in Figure 4a, the preamplifier signals are further processed by both shaping and timing amplifiers<sup>5</sup>. Output from the timing amplifier (TA) preserves rise-time information for distinguishing bulk and surface events (Section IV C 2). The shaping amplifier signals at 6  $\mu$ s shaping time (SA<sub>6</sub>) are optimized for energy measurement. The discriminator output provides the trigger instant for data acquisition (DAQ). Pulses from TA and SA<sub>6</sub> are digitized by 200 and 60 MHz flash analog-to-digital converters<sup>6</sup>, respectively. A typical SA<sub>6</sub> pulse at 4.2 keV<sub>ee</sub> for pPCGe is shown in Figure 4c.

## B. Data Samples

Characterizations of detector performance are carried out at our home-based laboratories. Physics measurements were made with the detectors placed inside the low-background facilities [7, 9] at Kuo-Sheng Reactor Neutrino Laboratory (KSNL) which has about 30 meter-water-equivalent overburden. Data of the Ge detector were recorded in conjunction with an NaI(Tl) anti-Compton (AC) detector and a cosmic-ray (CR) veto

scintillator array [7, 19, 20]. The NaI(Tl)-AC detector has a mass of 38.3 kg and a well-shaped geometry to enclose the Ge detectors. The entire setup is housed in a shielding structure. A background level of  $1 - 10 \text{ kg}^{-1} \text{ keV}_{ee}^{-1} \text{ day}^{-1}$  at the keV<sub>ee</sub>-range was achieved. The averaged pulse shapes of TA and SA<sub>6</sub> output due to different event categories are displayed in Figures 5a&b, respectively. The trigger instant from discriminator output of SA<sub>6</sub> is superimposed. It is defined by the time when the amplitude of SA<sub>6</sub> signals ( $A_{max}$ ) surpasses certain pre-set discriminator level ( $\Delta$ ). The trigger is therefore issued with a time delay of about 10  $\mu$ s at low energy relative to the prompt signals from TA, AC and CR.

Events at KSNL can be categorized by “AC<sup>-(+)</sup>⊗CR<sup>-(+)</sup>”, where the superscript <sup>-(+)</sup> denotes anti-coincidence(coincidence) with Ge signals. Physics events are those with genuine energy depositions in the Ge detectors.

A pure sample of physics events for calibration purposes can be collected by “AC<sup>+</sup>⊗CR<sup>+</sup>” tag where *all* three detectors are in coincidence. Candidate events of neutrino or WIMP-induced interactions are uncorrelated with other detectors and are therefore extracted from “AC<sup>-</sup>⊗CR<sup>-</sup>” tags.

At signal amplitude comparable to pedestal fluctuations, the AC<sup>-</sup>⊗CR<sup>-</sup> triggers are mostly due to self-trigger electronic noise. Positive fluctuations of these noise events in the shaped pulses of Figure 5b at the trigger instant are accompanied with negative fluctuations prior to and  $\sim$  20  $\mu$ s after the triggers. The corresponding TA pulse is shown in Figure 5a. It has a slow rise-time and also decreases in amplitude when the maximum is reached. This characteristic feature is expected because the self-trigger noise events originate from pedestal fluctuations rather than genuine energy depositions due to physics interactions at the detectors.

Self-trigger pedestal noise events are therefore, *in principle*, distinguishable from physics events by their different pulse shapes. However, it is technically challenging to devise efficient pulse-shape discrimination techniques at the event-by-event basis for physics signals with amplitude comparable to that of pedestal fluctuations. Developing advanced analysis algorithms for this task is beyond the scope of this report but continues to be our research efforts.

Random-trigger events are taken from random sampling of the pedestal baseline for monitoring and calibration purposes. They are useful for quantifying pedestal fluctuations, defining zero-energy offset and measuring DAQ dead-time and various efficiency factors.

Test-pulser events are produced by a precision pulse generator<sup>7</sup> fed to the preamplifier. Pulser signals probe the response of electronics system independent of the

<sup>3</sup> Custom-built for low electronics noise, Canberra Lingolsheim. Please contact the company for technical information.

<sup>4</sup> Model PSC954, Canberra Lingolsheim.

<sup>5</sup> Canberra 2026 and 2111, respectively.

<sup>6</sup> National Instruments PXI 5105 and PXI 5124, respectively.

<sup>7</sup> Precision Test Pulser National Instruments PXI 5412.

TABLE I: Summary table of performance parameters of Ge detectors in this study. The pulse maxima ( $A_{max}$ ) is adopted as energy estimator.

Performance Parameters	CoaxGe	ULEGe	pPCGe	nPCGe	Uncertainties (%) <sup>II</sup>
Modular Mass (g)	1000	5	500	500	—
RESET Amplitude (V)	N/A <sup>†</sup>	8.0	6.8	6.8	—
RESET Time Interval (ms)	N/A <sup>†</sup>	~700	~160	~170	—
Pedestal Noise					
Pedestal Profile RMS $\sigma_A$ (eV <sub>ee</sub> )	812	33	41	49	2.6
Area RMS $\sigma_Q$ (eV <sub>ee</sub> )	840	30	58	52	3.1
Pulsar Width					
FWHM (eV <sub>ee</sub> )	1566	87	110	122	1.5
RMS (eV <sub>ee</sub> )	665	37	47	52	1.5
X-Ray Line Width	Ga-K	<sup>55</sup> Fe	Ga-K	Ga-K	—
RMS (eV <sub>ee</sub> )	880	64	87	104	3.4
Electronic Noise-Edge for Raw Spectra (eV <sub>ee</sub> )	4900	220	228	285	1.8

<sup>II</sup> Uncertainties of pPCGe measurements are quoted as illustration. Other detectors have similar levels.

<sup>†</sup> Resistance feedback preamplifier is used in CoaxGe, so that the RESET timing structures are not-applicable (N/A).

TABLE II: Summary table of published performance parameters from previous studies on Ge detectors in which low energy threshold plays crucial roles.

Studies	Luke et al. [25]	IGEX [26]	CoGeNT [21]	MALBEK [24]	CDEX-1A [23]
Modular Mass (g)	800	2200	440	465	994
Pedestal Profile RMS $\sigma_A$ (eV <sub>ee</sub> )	115	—	69	70	51
X-Ray Line	—	Pb-X	Ga-K	Ga-K	Ga-K
Energy (keV <sub>ee</sub> )	—	75	10.4	10.4	10.4
Resolution RMS (eV <sub>ee</sub> )	—	340	111	117	91
Detector Threshold (eV <sub>ee</sub> )	700	4000	400	600	400

electron drifting effects for physics signals. As demonstrated in Figure 5b, pulser and physics events have identical profiles in SA<sub>6</sub>. Accordingly, pulser events can be used for studying the detector energy response (Section III C) and measuring trigger efficiency (Section IV B 2), because both measurements are defined by the SA<sub>6</sub> pulses. However, as depicted in Figure 5a, pulser signals have faster rise-time than physics events (bulk samples tagged with “AC<sup>+</sup>⊗CR<sup>+</sup>”) in their TA output. It would be unjustified to adopt test-pulser events for efficiency calibrations that involve pulse-shape analysis of TA signals, such as in the identification of bulk/surface events (Section IV C 2i).

We note that different test-pulser models, or the same model under different settings, give different TA output. The pulser profile of Figure 5a is due to a setting that gives the closest match to that of physics events. Detailed understanding and optimization of pulser parameters for making TA output compatible with physics signals are beyond the scope of this work, but represent a relevant direction of future research.

The linearity of test-pulser output with respect to input setting ( $A_{Pulser}$ ) is verified by direct measurement of raw pulser signals, as depicted in Figure 6. Super-

imposed are the energy-equivalent settings for electronic noise-edges of pPCGe and nPCGe, as well as the nominal range specified in factory data-sheet, demonstrating the validity of pulser measurements for our current studies.

## C. Energy Measurement

### 1. Pedestal Noise Characterization

The pedestal electronic noise of detectors are described by “Pedestal-Noise-Profile-RMS” ( $\sigma_A$ ) and “Noise-Area-RMS” ( $\sigma_Q$ ) derived from random-trigger events. The RMS (Root-Mean-Square) of pedestal areas integrated over  $[t_{start}, t_{end}]$  is  $\sigma_Q$ , while the bin-by-bin pedestal signal profile distributions of random-trigger events give  $\sigma_A$ .

There are various merits in choosing  $\sigma_A$  as a key variable. As we shall see in subsequent sections, various detector behaviors can be described by universal functions when energy scales are expressed in units of  $\sigma_A$ . In addition, measurements of  $\sigma_A$  in calibrated energy unit provide a quick-and-valid comparison of noise levels among different detectors.

The pedestal noise levels of detectors studied in this

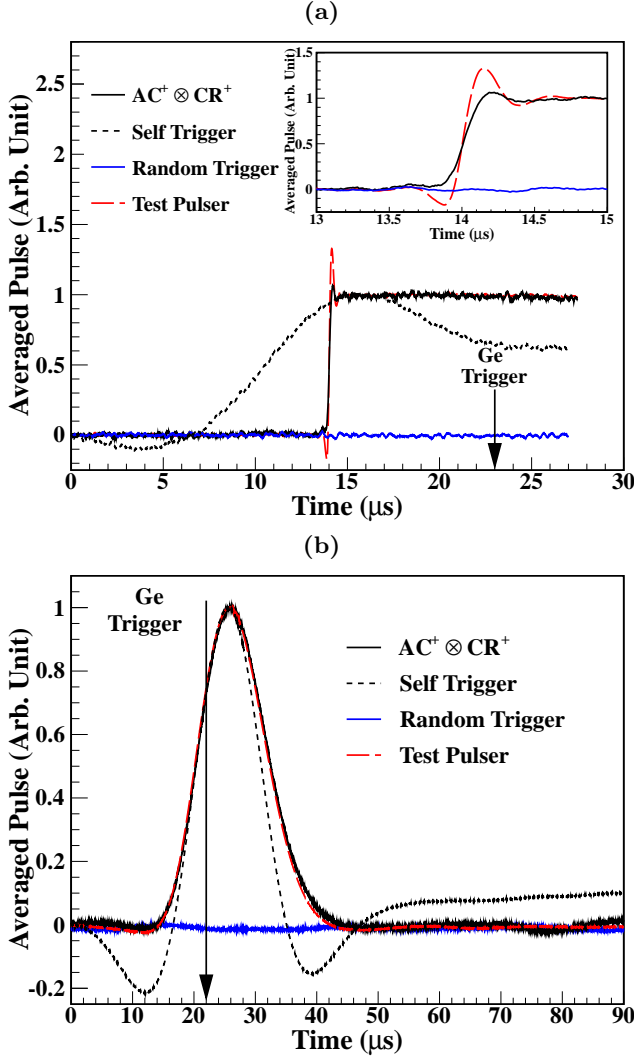


FIG. 5: Comparison of averaged pulse shapes from (a) timing amplifier TA and (b) shaping amplifier SA<sub>6</sub> for events due to random-trigger (blue solid), self-trigger pedestal electronic noise (black dashed), test-pulser (red dashed) and physics interactions (black solid). Data from pPCGe are used as illustrations. The selected events except random-trigger ones are of effective energy near noise-edge ( $\sim 300$  eV<sub>ee</sub> in this example). Their amplitude is normalized to unity in the display, except for random-trigger events whose normalization follows that of self-trigger events. The physics samples are from bulk events tagged with “AC<sup>+</sup> ⊗ CR<sup>+</sup>” and after basic filters of Section IV C 1. The trigger instants defined by Ge-SA<sub>6</sub> signals are shown. The physics and test-pulser events are identical in SA<sub>6</sub> but differ in TA. The physics and self-trigger noise events show different profiles in both amplifiers and are therefore, *in principle*, distinguishable.

work are summarized in Table I.

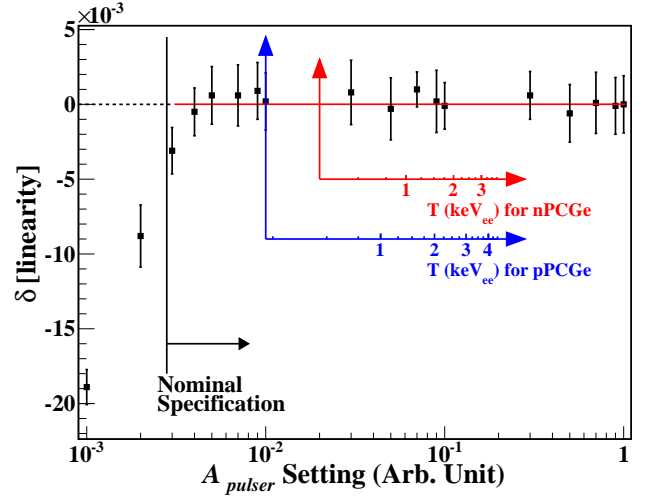


FIG. 6: Direct measurement of linearity of test-pulser output relative to input setting ( $A_{pulser}$ ). Superimposed are the nominal range specified by the manufacturer. Corresponding energy scales in keV<sub>ee</sub> above electronic noise-edges of pPCGe and nPCGe are also shown. Deviations from linearity are described by  $\delta[\text{linearity}]$ , which is the fractional deviations of measured amplitude from the nominal values.

## 2. Energy Estimator

As illustrated in Figure 4c,  $A_{max}$  and  $Q_{area}$  of SA<sub>6</sub> are defined in our studies as maximal amplitude and integrated area within the time window  $[t_{start}, t_{end}]$ , respectively. The averaged pedestal level is an offset and is subtracted. Extensive studies have confirmed that the selected amplifier shaping time (6  $\mu$ s) and integration interval (30  $\mu$ s) would produce the best detector performance.

Conventional applications of Ge detectors are at an energy range where  $Q_{area}$  and  $A_{max}$  are substantially above  $\sigma_Q$  and  $\sigma_A$ , respectively. Both parameters have been adopted to estimate the energy of an event. When signal amplitude becomes comparable to magnitude of electronic noise in low-energy applications, further investigations are necessary.

For instance, when physics signals far exceed pedestal noise (as in, for instance, imaging applications or double beta decay experiments), there are established software techniques for shaping the fast TA pulse [27], and extracting the pulse amplitude information from the shaped output. This approach, however, is limited in accuracy, efficiency and robustness when the signals are only several times larger than the pedestal noise – the range of interest in this work.

Measurements show  $\sigma_A \lesssim \sigma_Q$  for the detectors studied in this work, as listed in Table I. Pulse amplitude provides a better estimator of energy than its area. Accordingly, the SA<sub>6</sub> amplitude  $A_{max}$  is adopted for energy measurement. The details of energy response are discussed in Section III C 4.

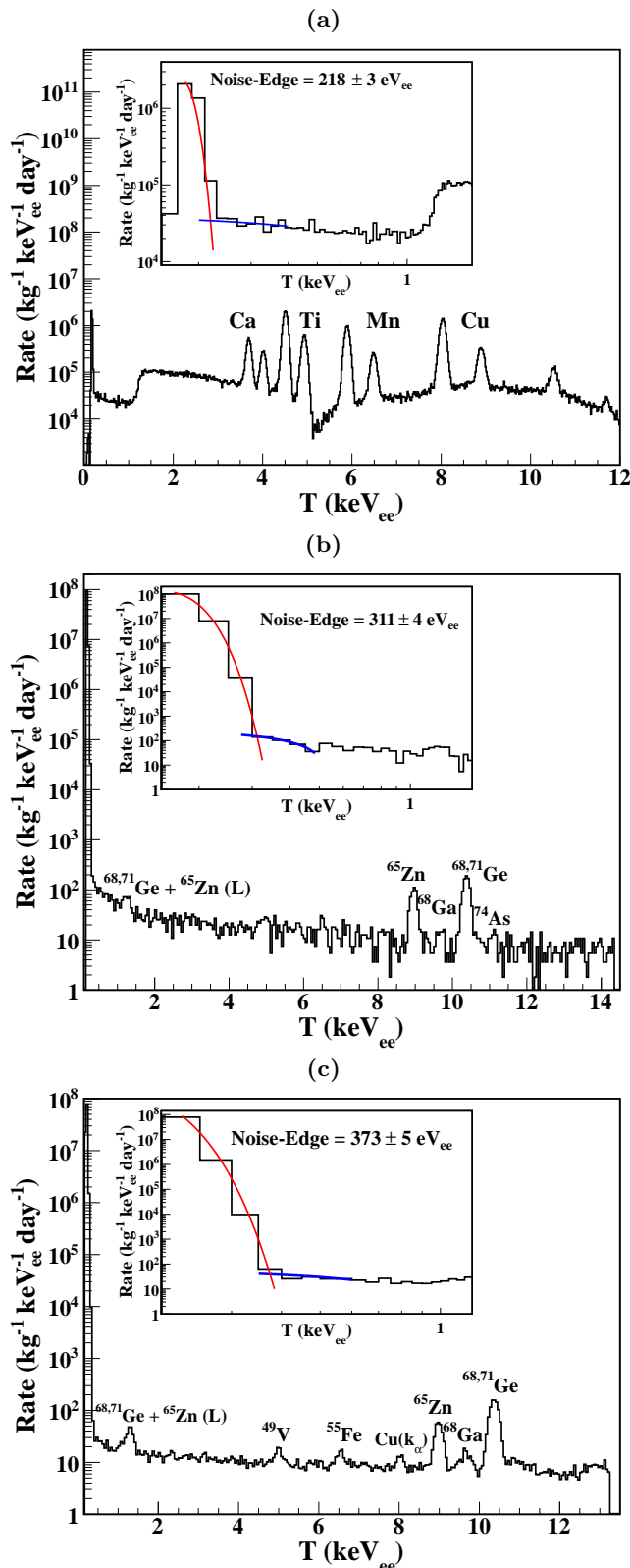


FIG. 7: Typical (a) ULEGe, (b) pPCGe and (c) nPCGe spectra showing X-ray peaks and noise-edges. The lines in all cases are used in energy calibration. ULEGe is an n-type detector with a thin surface layer. It is also equipped with a thin cryostat window which allows detection of external X-ray lines in (a). The two PCGe detectors were built for applications with low count rates and therefore do not have thin windows. The peaks are due to electron capture in isotopes which are cosmogenically activated and emit X-rays inside the detectors. Both (b) and (c) are spectra for events after basic filters and with  $AC^- \otimes CR^-$  tags. The noise-edges are illustrated in the insets, defined as the energy at which physics signals would dominate self-trigger electronic noise events.

In addition, the DAQ trigger is issued when  $A_{max}$  exceeds discriminator threshold  $\Delta$ . Various aspects of the trigger are discussed in Section IV B.

### 3. Energy Calibration

Shown in Figures 7a,b&c are the measured spectra of ULEGe, pPCGe and nPCGe, respectively.

The outer boron-implanted dead surfaces of n-type Ge detectors (such as ULEGe, nPCGe) are thin ( $\mathcal{O}(1 \mu m)$ ). In addition, ULEGe is equipped with a thin window made of carbon composite materials. It was calibrated by an external X-ray generator<sup>8</sup> which induces emissions from different elements placed close to the detector, and gives rise to the characteristic X-ray peaks [19, 22] depicted in Figure 7a. The step at  $\sim 1 \text{ keV}_{ee}$  is due to attenuation of low-energy photons by the thin window.

The *in situ* background spectra at KSNL for pPCGe and nPCGe are displayed in Figures 7b&c, respectively. The  $n^+$  surface electrodes of p-type Ge detectors are fabricated by lithium diffusion and have a typical thickness of  $\sim 1 \text{ mm}$  [28]. Therefore, external  $\gamma$ 's with energy less than 50 keV are totally suppressed and cannot be used. Instead, calibration is provided [20, 21, 23] by internal cosmogenic radioactivity, the strongest of which are peaks from electron capture of  $^{68,71}\text{Ge}$  producing Ga X-rays (10.37 keV and 1.29 keV). This calibration scheme also applies to nPCGe which does not have a thin entrance window and is housed in a copper cryostat of 1 mm thickness.

In all the detectors studied, no physics-related structures are observed below  $\sim 1 \text{ keV}_{ee}$ , where energy calibration is performed using the test-pulsar. Data were taken with decreasing pulser amplitude. Pulser measurements at zero-amplitude are equivalent to random-trigger events. The energy scale of the pulser is defined by matching to the  $\gamma$ -peaks at high energy. As demonstrated in Figure 6, the intrinsic pulser response is linear at the range corresponding to physics events. The resolution function at sub-keV energy is derived via extrapolating measured widths of X-ray peaks at high energy.

The pulser measurements for pPCGe and nPCGe are displayed in Figure 8a. Polynomial functions provide calibration of  $A_{max}$  into energy unit over the entire range. In particular, the response is linear at the physics region of interest above the electronic noise-edge.

### 4. Energy Response

Deviations from linearity in  $A_{max}$  can be expected when pulse amplitude is comparable to pedestal noise

<sup>8</sup> X-Ray Generator: Ampetek Cool-X



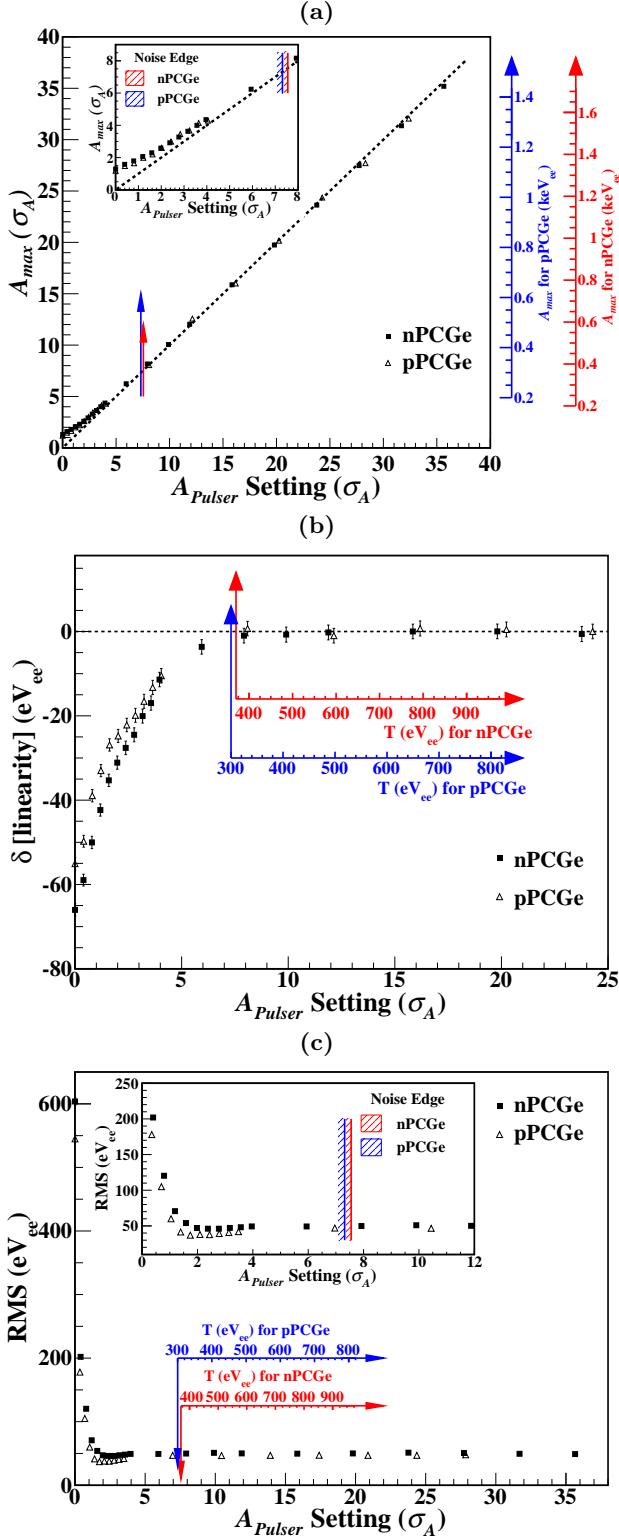


FIG. 8: Response of pPCGe and nPCGe versus energy when the test-pulser amplitude is comparable to pedestal noise fluctuations – (a) energy estimator  $A_{max}$ , (b) deviations from linearity, and (c) RMS resolution. The energy scales are in  $\sigma_A$  unit to illustrate universal behavior, and in  $\text{eV}_{ee}$  unit for specific detectors above their noise-edges. It can be seen that the detector responses are well-behaved in the physics regions of interest, but become anomalous as the input approaches zero.

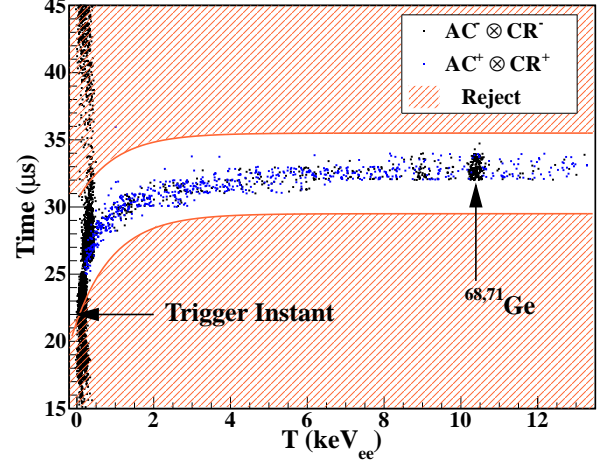


FIG. 9: Timing correlation of maximal pulse location ( $t_{max}$  of Figure 4c) relative to trigger instant. Data from nPCGe are used as illustrations.

fluctuations. This is a consequence of using pulse amplitude as energy estimator – even random sampling of the pedestal noise would give finite values of  $A_{max}$ . However, as shown in Figure 8b, the response is non-linear only at  $A_{max} < 6 \sigma_A$  for both detectors. At the region of interest above the electronic noise-edge of  $7.3(7.6) \sigma_A$  for pPCGe(nPCGe), the response is linear with deviations  $< 4 \text{ eV}_{ee}$ , justifying the validity of the amplitude measurement.

Energy resolution of pulser-events is a good parameter for characterizing the contributions of electronics system and for comparing the performance of different detectors, thereby providing complementary and independent information to  $\sigma_A$  from pedestal noise. The RMS resolution for test-pulser input is shown in Figure 8c. The energy response deteriorates at  $A_{max} < 1.2 \sigma_A$ , which is below the electronic noise-edge and physics region of interest.

The energy response varies with search time intervals after the trigger instant, in which  $A_{max}$  is located. The mean time difference between  $A_{max}$  and the trigger instant is depicted in Figure 9. There is a shift of the maximum timing at low energy, because the trigger instant is defined by a constant-voltage discriminator level.

The distributions of  $A_{max}$  and their RMS with random pedestal events (equivalent to pulser events with  $A_{Pulser} = 0$ ) as function of search time intervals are displayed in Figure 10a&b, respectively. Shorter intervals would extend the linearity range to lower energy but deteriorate energy resolution. In the limiting case when a single time-bin is taken to define the pulse maximum (that is, when the search time interval approaches zero),  $A_{max} = 0$  and  $\text{RMS}[A_{max}] = \sigma_A$  for random-trigger events and the energy response is linear down to zero-energy, as expected. The selected intervals for analysis in this work are marked.

The fiducial volume of pPCGe corresponds to the region giving rise to “Bulk” events (to be described in Sec-

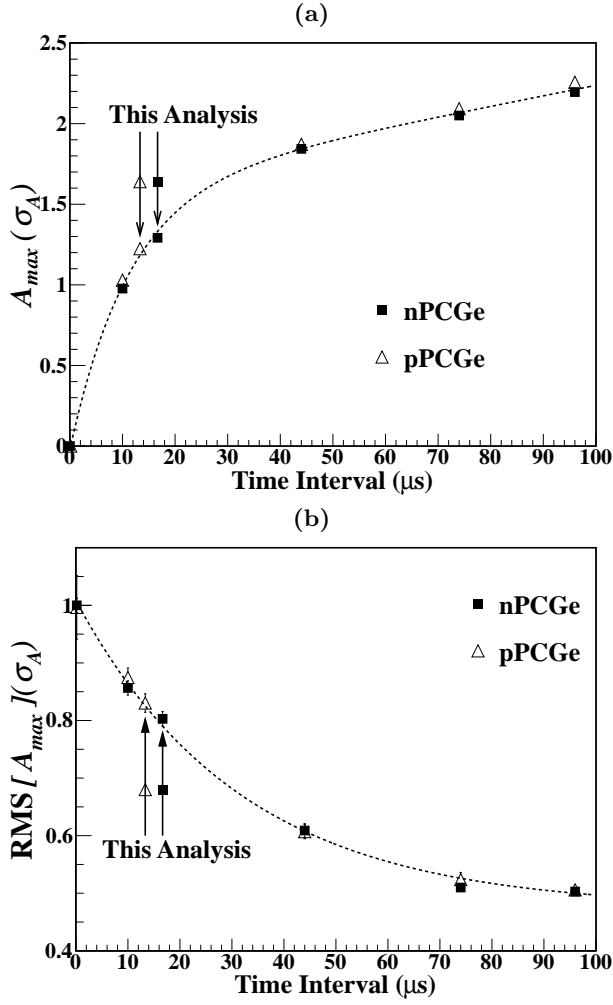


FIG. 10: (a) Pulse amplitude  $A_{max}$  and (b) RMS distributions of random pedestal events as function of search time intervals after trigger instant during which the maximal amplitude is located. The dotted lines are fits of combined data showing universal behavior independent of detectors. The selected intervals for the analysis in this work are marked.

tion IVC 2i) while that of nPCGe is the entire active detector, minus the  $p^+$  surface electrode of micron-level thickness and the  $\sim mm^3$  volume around the  $n^+$  point-contact. Physics events originated at different locations of the detector fiducial volume exhibit the same response, as discussed in Section IVC 2ii. This justifies the adoption of physics background events with  $AC^+ \otimes CR^+$  (plus “Bulk” tag for pPCGe) to characterize *in situ* detector behavior and to measure efficiencies of neutrino- and WIMP-induced signals in  $AC^- \otimes CR^-$ , although their spatial locations within the detectors are in general not identical.

The current scheme of energy measurement with the amplitude of  $SA_6$  is therefore applicable to the entire detector fiducial volume. It is robust and well-behaved in the energy range corresponding to physics events.

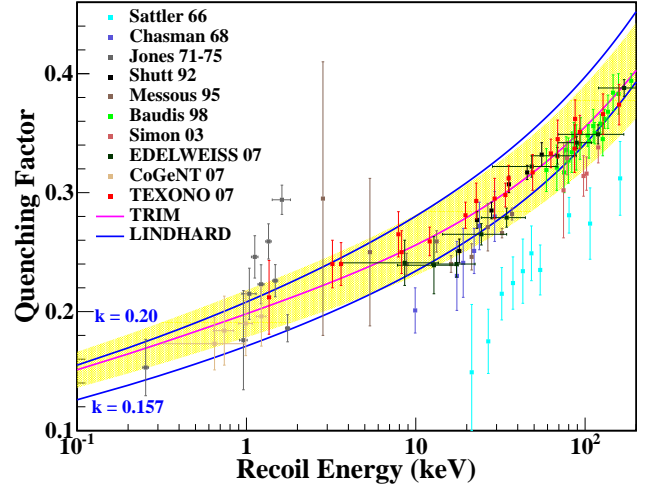


FIG. 11: Summary of QF studies on Ge detectors. Derived values obtained using the TRIM software package [29] and the Lindhard theory [30] in two parametrizations are superimposed to the measurements. Selection of the TRIM-QF curve with 10% systematic uncertainty (yellow band) provides good description of the current knowledge over a large energy range. Readers are advised to refer to the color version which presents better the wealth of information.

#### D. Quenching Factor

Quenching factor (QF) is the ratio of ionization energy to the nuclear recoil energy deposited by radiations. In Ge detectors, ionization energy corresponds to the amount of electron-hole pairs created. Knowledge of QF is essential in studies on  $\nu N$  and  $\chi N$  processes in Ge ionization detectors, the signatures of which are due to nuclear recoils.

A compilation of existing QF measurements in Ge [4] is given in Figure 11. Superimposed are calculations obtained using the TRIM software [29] and the Lindhard model [30] at two popular parametrizations ( $k=0.157$  and  $0.20$ ). Both schemes have been used in various dark matter experiments. The TRIM results explain the QF data at a larger energy range and were adopted in our previous analysis with an assigned systematic uncertainty of 10% [19, 20, 22, 23]. As illustrated by the yellow band of Figure 11, this choice accounts well the spread of measured data and the two Lindhard parametrizations. Constraints on  $\chi N$  cross-sections were selected from the most conservative results within the uncertainty band.

### IV. SIGNAL SELECTION AND EFFICIENCY

#### A. Overview

Signal events have to survive various selection criteria (“cuts”) applied to the raw data. The survival probability or signal efficiency of each of these cuts must be known

in order to correctly extract the physics information.

1. Trigger – The physics events produce trigger signals for the DAQ system. Trigger efficiency ( $\varepsilon_{\text{Trig}}$ ) is energy-dependent. Its evaluation is discussed in Section IV B 2.
2. DAQ – The trigger signal activates the DAQ system which subsequently records a complete event. DAQ efficiency ( $\varepsilon_{\text{DAQ}}$ ) is energy-independent. It can be accurately evaluated by the ratio of random-trigger events recorded in the DAQ computer to the number of trigger signals issued.

This efficiency factor is associated with the “DAQ dead-time” – the fraction of time in which the DAQ system is not actively responding to the trigger, through the relation [DAQ Dead Time =  $1 - \varepsilon_{\text{DAQ}}$ ].

3. Analysis – The objectives of offline analysis procedures are to retain physics signals and suppress background events. Some of the signal events may be rejected in the processes, therefore giving rise to efficiency factors which are generally energy-dependent.

In this work, the offline analysis can be further classified into three categories according to their different characteristic features listed as follows.

- (a) Physics signals in Ge are selected using information from different detector components which are the CR and AC detectors for KSNL measurements. Neutrino- and WIMP-induced signals in Ge are uncorrelated (that is, in anti-coincidence) with these detectors. The selected anti-coincidence interval in software analysis is  $4.5 \mu\text{s}$ . The signal efficiencies ( $\varepsilon_{\text{CR}}$  and  $\varepsilon_{\text{AC}}$ ) can be accurately measured with the survival fractions of random-trigger events subjected to the identical selection cuts. Measurements with experiments at KSNL [7, 19, 20] give  $\varepsilon_{\text{CR}} \simeq 93\%$  and  $\varepsilon_{\text{AC}} > 99\%$ .
- (b) Physics signals are due to genuine charge depositions. They can be distinguished from self-trigger noise events by differences in their pulse shape and timing. The signal efficiencies can be derived from the survival probabilities of  $\text{AC}^+ \otimes \text{CR}^+$  samples.

We present several selection criteria with general applicability to all detectors in Section IV C 1, where their combined efficiency is denoted by  $\varepsilon_{\text{bf}}$ . Advanced algorithms with goals of extracting physics signals *below* the noise-edge are being pursued.

- (c) Events due to neutrino and WIMP interactions are mostly located in the bulk of the detectors while background events from low-energy ambient radioactivity deposit their energy primarily at the surface. These events

differ in their rise-time in pPCGe [31]. Selection of bulk events requires pulse-shape analysis. Special calibration schemes are devised to evaluate the signal efficiency and background contamination factors [3].

We emphasize that, in order to avoid bias, a single energy measurement scheme ( $A_{\text{max}}$  as defined in Figure 4c) should be used exclusively and consistently throughout the sequence of selection cuts and efficiency evaluation.

## B. Trigger and Data Acquisition

### 1. Trigger Rates

Trigger instant is defined as the time at which  $\text{SA}_6$  amplitude  $A_{\text{max}}$  exceeds the discriminator level  $\Delta$ . When the amplitude of pedestal fluctuations follows a Gaussian distribution, the trigger rate is given by [32]:

$$R \sim \frac{1}{4 \tau_S} \exp \left[ -\frac{1}{2} \left( \frac{\Delta}{\sigma_A} \right)^2 \right], \quad (3)$$

where  $\tau_S$  is the shaping time and  $\sigma_A$  is the RMS of pedestal fluctuation. Measurements of random-trigger events show there is on average one positive fluctuation per  $4 \tau_S$ , verifying the normalization of Equation 3.

The measured trigger rates as a function of  $\Delta$  are displayed in Figure 12a, showing consistency with predictions at  $\Delta > 3.3 \sigma_A$  and implying that the pedestal noise fluctuations are indeed Gaussian. Deviations at small  $\Delta$  can be quantitatively accounted for by the finite width of inactive interval after a valid trigger, such that accidental triggers within the gate interval are counted as a single event. In addition, all the detectors exhibit consistent behavior, indicating that Equation 3 is universal when the energy scale is expressed in  $\sigma_A$  unit. As illustrated in the inset of Figure 12a, various modes of “other electronics noise” (such as microphonics and RESET-induced events) are the main contributors at low energy above pedestal noise fluctuations, while physics events would dominate the trigger rates at large  $\Delta$ .

The evaluation of electronic noise-edge values from measured energy spectra is illustrated in the insets of Figures 7a,b&c. The self-trigger noise events are due to tails in Gaussian fluctuations. The noise-edge corresponds to the energy above which physics events dominate over electronic noise. Accordingly, the noise-edge is not a constant but varies with physics event rates. This is depicted in Figure 12b for the various detectors at different event rates due to different background configurations. The measurements demonstrate that, in a given detector, lower physics event rates give rise to higher noise-edge levels. The noise-edge at KSNL after  $\text{AC}^- \otimes \text{CR}^-$  selection corresponds to  $\sim 7 \sigma_A$ .

In this study, the  $\text{SA}_6$  amplitude  $A_{\text{max}}$  is the relevant quantity for defining online trigger and for providing energy measurement. Advances in real-time pulse-shape

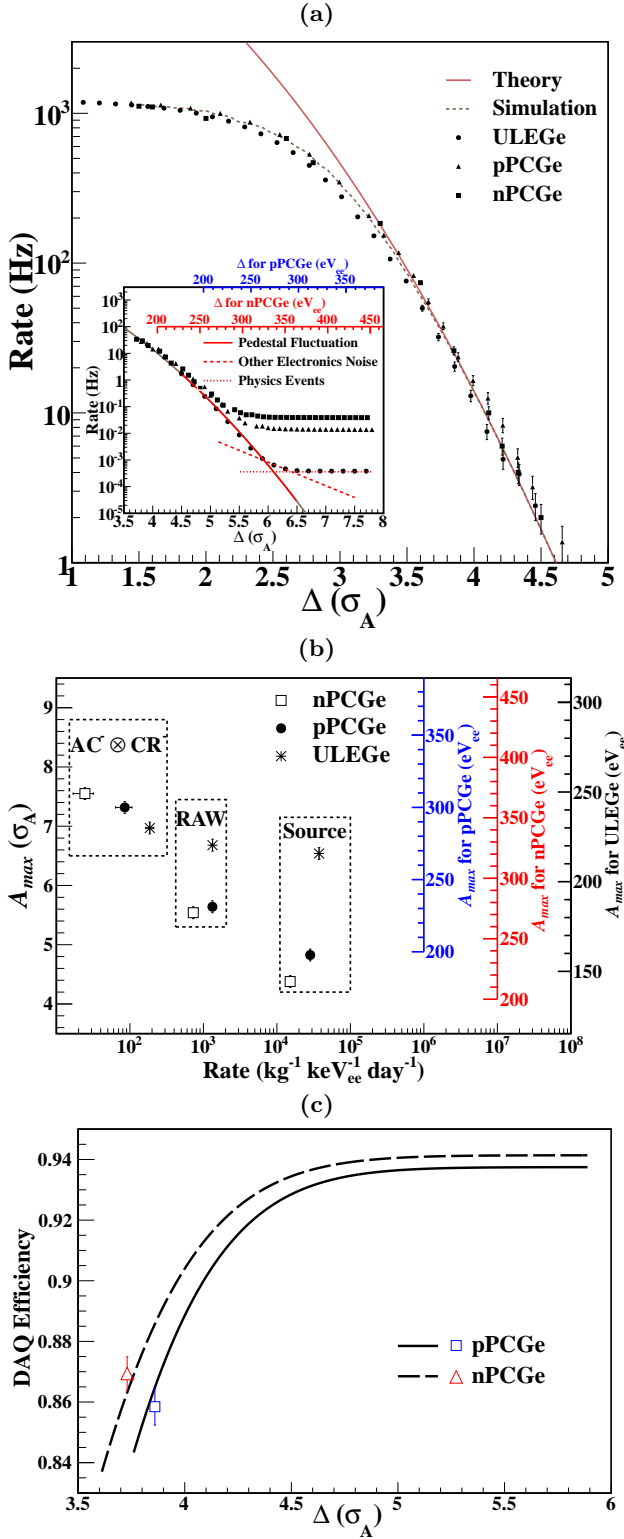


FIG. 12: (a) Measured trigger rates as a function of discriminator threshold  $\Delta$ , showing a universal behavior of self-trigger pedestal noise when expressed in  $\sigma_A$  unit. The origins of deviations at high and low  $\Delta$  are explained in the text. The energy scales for the specific detectors in eV<sub>ee</sub> are also shown. (b) Noise-edge versus rates of physics event for various detectors and at different background configurations: (i) high rates with radioactive sources, (ii) raw rates at low-background configurations at KSNL, and (iii) after AC<sup>−</sup>⊗CR<sup>−</sup> selection. The data demonstrate that lower event rates correspond to higher noise-edge levels for the same detectors. (c) Data acquisition efficiencies – the expectation follows directly from (a) using as input the average DAQ dead-time per event and the post-RESET veto windows. Measurements are provided by random trigger events.

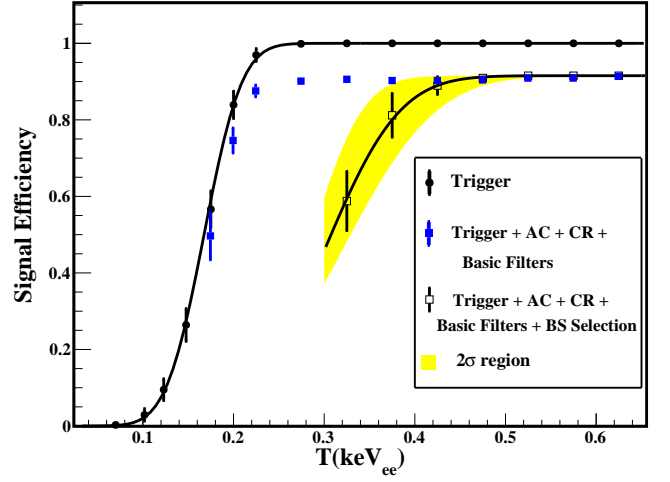


FIG. 13: Various analysis efficiency factors for pPCGe in this work. Efficiencies before and after bulk-event BS-selection are shown. The signal efficiency for nPCGe is a step function smeared by energy resolution at trigger level of 204 eV<sub>ee</sub>. The displayed data do not include readout efficiency factors due to DAQ dead time.

processing in Field Programmable Gate Arrays (FPGA) make it possible to have other sophisticated and more efficient trigger schemes. This line of research is being pursued, with the goals of improving the DAQ dead time and reducing computing overhead. The measured detector performance parameters reported in this article, however, are independent of trigger configurations and DAQ systems being adopted.

## 2. Trigger and Data Acquisition Efficiencies

In this analysis where both trigger timing and energy measurements are defined by the amplitude of the SA<sub>6</sub> pulse,  $\varepsilon_{\text{Trig}}$  is a step function at  $\Delta$  smeared by energy resolution. Measurements are provided by the test-pulser data, where  $\varepsilon_{\text{Trig}}$  is the fraction of events giving trigger signals. The measurements are depicted in Figure 13 for pPCGe. In practice, trigger rates are set to 1–10 Hz corresponding to  $\Delta \sim 4.6 - 4.1 \sigma_A$ , respectively. This  $\Delta$ -range is lower than the typical electronic noise-edge at  $\sim 5 - 6 \sigma_A$ , such that  $\varepsilon_{\text{Trig}}$  does not play a role in the physics analysis.

The DAQ dead-time corresponds to two circumstances: (i) in a certain pre-set time window (typically 10 ms) after the preamplifier RESET, and (ii) during data transfer to the computer hard disk (typically 2 ms per event).

The expected evolution of  $\varepsilon_{\text{DAQ}}$  with  $\Delta$  in Figure 12c follows directly the measured trigger rates of Figure 12a, using as input the average DAQ dead-time per event and the post-RESET veto windows. Direct measurements with ratios of recorded events to number of random-triggers issued to the DAQ system are superimposed, showing excellent agreement. At large  $\Delta$ ,  $\varepsilon_{\text{DAQ}}$  is con-

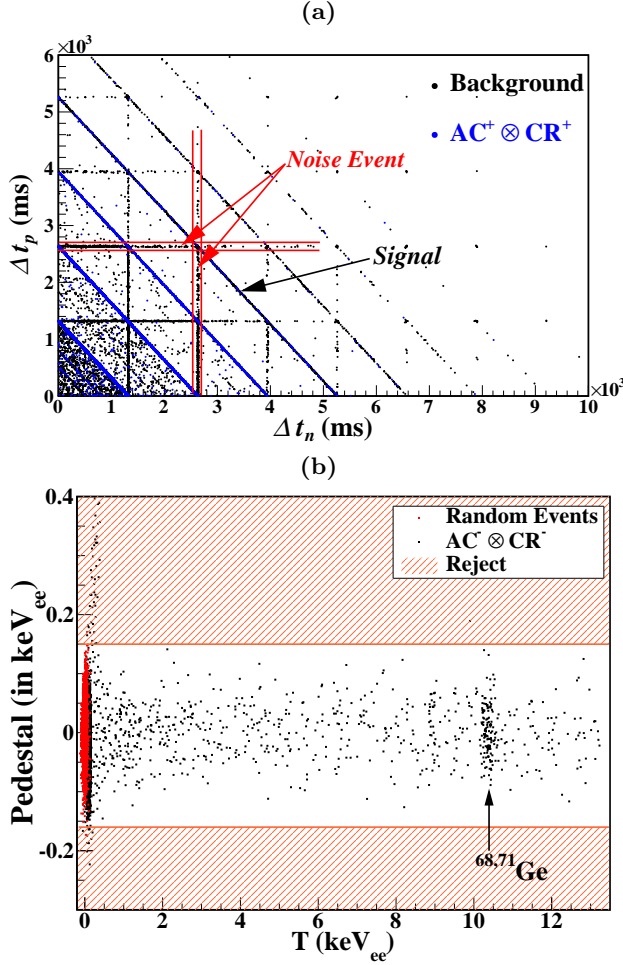


FIG. 14: Basic filter selections, provided by (a) timing within a RESET period ( $\Delta t^+$  and  $\Delta t^-$  of Figure 4b), and (b) pedestal fluctuations. An additional selection is on the timing of SA<sub>6</sub> maxima, displayed in Figure 9. “Reject” parameter spaces are shown as shaded regions. Data from pPCGe and nPCGe are used as illustrations in (a) and (b), respectively.

stant and defined by the post-RESET veto time. Variations in the constant level among detectors can be attributed to differences in RESET time intervals.

### C. Signal Events Selection

The exact selection procedures and efficiency derivations for physics signals, though differ in details for each detector and in each analysis, share many common features.

#### 1. Basic Filters

RESETs from preamplifiers induce electronic noise which gives rise to self-trigger events. As depicted in Figure 14a, these background events can be identified

via correlations in timing with the previous and next RESETs ( $\Delta t^-$  and  $\Delta t^+$ , respectively, as defined in Figure 4b). There is a natural RESET period for every detector (which is  $\sim 1.3$  s in this example of pPCGe with an earlier preamplifier model<sup>9</sup>). Most physics signals populate the dominant diagonal bands at low- $(\Delta t^+, \Delta t^-)$ . Events at those longer-period bands correspond to situations where the previous or next RESETs are not recorded when they fall in the DAQ dead-time intervals. Some RESETs would be issued prior to their natural period when they are induced by electronics instabilities or when the detector is saturated by large charge depositions, such as direct hits of cosmic-ray muons. RESET-induced noise events are the horizontal and vertical bands on the plot, and can be completely rejected.

Other electronic noise events include those induced by the tails of earlier signals. Characterized by an anomalous pedestal level prior to the trigger instant, these noise events can be efficiently identified and rejected, as demonstrated in Figure 14b.

The timing of the SA<sub>6</sub> maxima, depicted in Figure 9, is another effective selection criterion.

The corresponding signal efficiencies  $\varepsilon_{bf}$  are derived. For the  $\Delta t^+ - \Delta t^-$  selection of Figure 14a,  $\varepsilon_{bf} > 97\%$ , given by the survival fraction of  $AC^+ \otimes CR^+$  physics events when subjected to identical criteria. The selection of pedestal range illustrated in Figure 14b has  $\varepsilon_{bf} > 99\%$ , given by random-trigger events. The selection of pulse maxima shown in Figure 9 has  $\varepsilon_{bf} > 99\%$ , derived also with  $AC^+ \otimes CR^+$  physics events. These calibration events are also displayed in the respective figures.

#### 2. Pulse-Shape Analysis on Event Rise-Time

Electron-hole pairs produced at the surface (S) layer in pPCGe are subjected to a weaker drift field than those in the bulk volume (B). A fraction of the pairs will recombine while the residuals will induce signals which are weaker and slower than those originated in B. The S-events would therefore exhibit slower rise-time and partial charge collection compared to B-events [31]. This effect becomes relevant to the selection of neutrino- and WIMP-induced signals at sub-keV energy. Quantitative studies on these detector features, the differentiation of S and B events by pulse-shape analysis and the calibration schemes which provide measurements of signal-retaining and background-suppression efficiencies ( $\varepsilon_{BS}, \lambda_{BS}$ ) are discussed in detail in Ref. [3]. We present new results on both pPCGe and nPCGe in what follows.

#### (i) Bulk versus Surface Events in pPCGe

The rise-time of the TA-signal ( $\tau$ ) is parametrized

<sup>9</sup> Model PSC921, Canberra Lingolsheim.



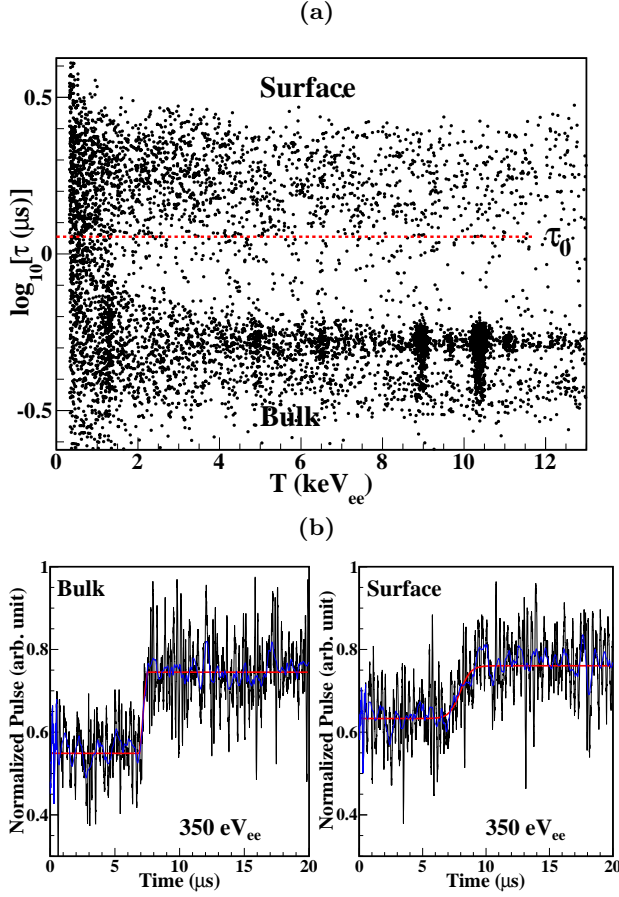


FIG. 15: (a) TA  $\tau$ -distribution in pPCGe with low background at KSNL. The selection criterion of B signal events is defined by the cut at  $\tau_0$ . (b) Typical TA pulses for B and S events near threshold for pPCGe.

by the hyperbolic tangent function

$$\frac{1}{2} A_0 \times \tanh\left(\frac{t - t_0}{\tau}\right) + P_0, \quad (4)$$

where  $A_0$ ,  $P_0$  and  $t_0$  are the amplitude, pedestal offset and timing offset, respectively. The  $\tau$ -distribution of pPCGe events with  $AC^- \otimes CR^-$  tags is displayed in Figure 15a. At high energy where electronic noise is negligible, the fits are in excellent agreement with data (with a mean  $\chi^2/\text{dof}$  of 64.7/64), showing that Equation 4 is an appropriate description of the rise-time of physics events.

Typical B and S events near noise-edge are illustrated in Figure 15b. At low energy, the cross-contaminations between the two samples must be taken into account. The efficiency-corrected bulk and surface rates ( $0, S_0$ ) are related to measured rates (B, S) via:

$$\begin{aligned} 0 &= \frac{\lambda_{BS} \cdot B - (1 - \lambda_{BS}) \cdot S}{(\varepsilon_{BS} + \lambda_{BS} - 1)} \\ S_0 &= \frac{\varepsilon_{BS} \cdot S - (1 - \varepsilon_{BS}) \cdot B}{(\varepsilon_{BS} + \lambda_{BS} - 1)}. \end{aligned} \quad (5)$$

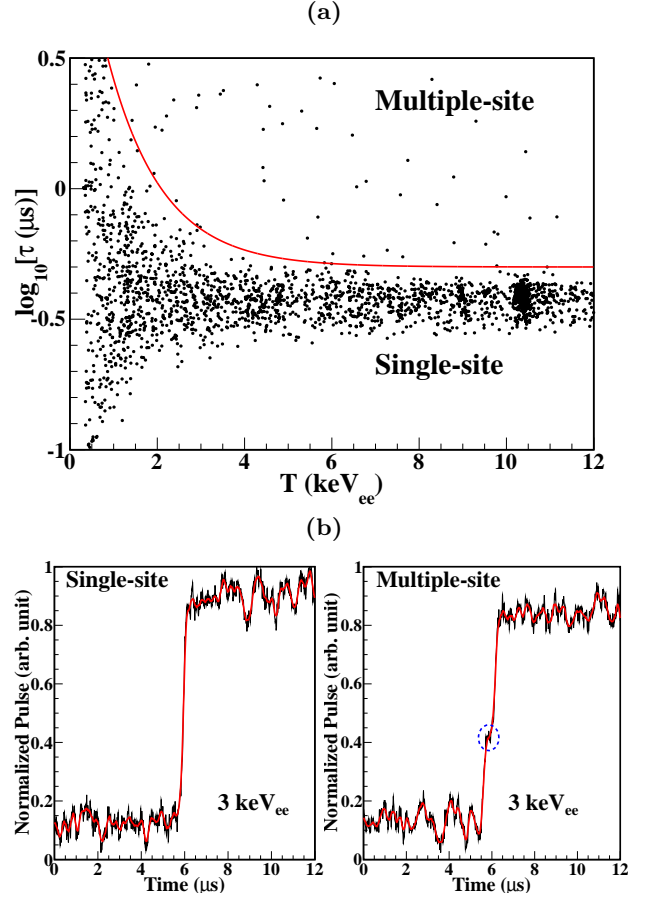


FIG. 16: (a) TA  $\tau$ -distribution in nPCGe with low background at KSNL, showing a dominating band due to single-site events in the detector bulk. Scattered “slow- $\tau$ ” events away from the band are from multiple-site energy depositions. Anomalous surface events are negligible. (b) Typical TA pulses showing single- and multiple-site events for nPCGe. Multiple-site events are characterized by kinks in rise-time profiles like the one marked in blue circle.

Two components contribute to  $0(S_0)$ . The first positive term accounts for the loss of efficiency in the measurement of  $B(S)$ , while the second negative term corrects mis-identification due to leakage effects. Both  $(\varepsilon_{BS}, \lambda_{BS})$  factors should be properly accounted for in order to provide correct measurements of the energy spectra for bulk events.

Systematic uncertainties in the derivation of  $(\varepsilon_{BS}, \lambda_{BS})$  originate from the choice of parameters such as the cut-value  $\tau_0$ , and from differences in detector response between the calibration sources and physics background. However, the combined systematic and statistical errors of  $(\varepsilon_{BS}, \lambda_{BS})$ , as well as the efficiencies of other cuts, play only minor roles in the overall uncertainties. In low count-rate experiments, the leading contributions remain the statistical errors in physics measurements [3, 20, 23]. These are further boosted by the

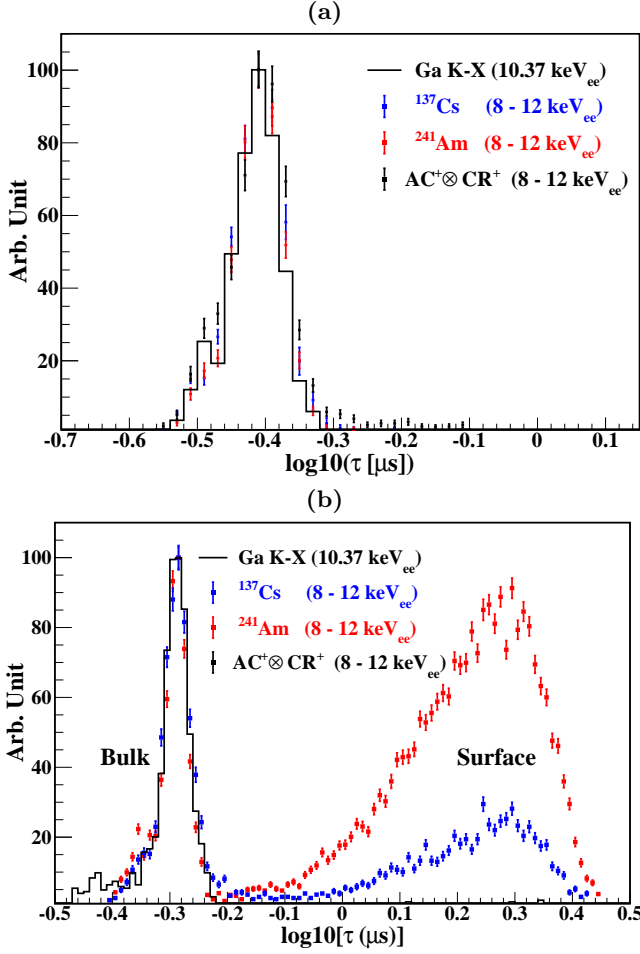


FIG. 17: TA  $\tau$ -distributions of  $^{241}\text{Am}$ ,  $^{137}\text{Cs}$ ,  $\text{AC}^+ \otimes \text{CR}^+$ , and Ga K-shell X-rays events in (a) nPCGe and (b) pPCGe. There are no anomalous surface events in nPCGe. Bulk-to-Surface event ratios in pPCGe are different, because different sources give rise to events with different spatial distributions in the detector. Bulk distributions for all sources are consistent in both detectors, demonstrating uniform timing response over the entire detector fiducial volume.

$1/(\varepsilon_{\text{BS}} + \lambda_{\text{BS}} - 1)$  factor of Equation 5 as  $(\varepsilon_{\text{BS}}, \lambda_{\text{BS}})$  deviate from unity at low energy.

In contrast, anomalous surface events in nPCGe are negligible, as indicated in Figure 16a where the S-band is absent. Scattered events on the “slow- $\tau$ ” side away from the B-events are due to charge depositions in multiple sites. Typical single- and multiple-site events at low energy are illustrated in Figure 16b.

For completeness, we note that pulse-shape analysis on fast TA signals in pPCGe is also an important technique in double beta decay experiments [33]. Single- and multiple-site events at the MeV range are distinguished by comparing amplitude and energy of the fast TA pulse.

## (ii) Uniformity within Fiducial Volume

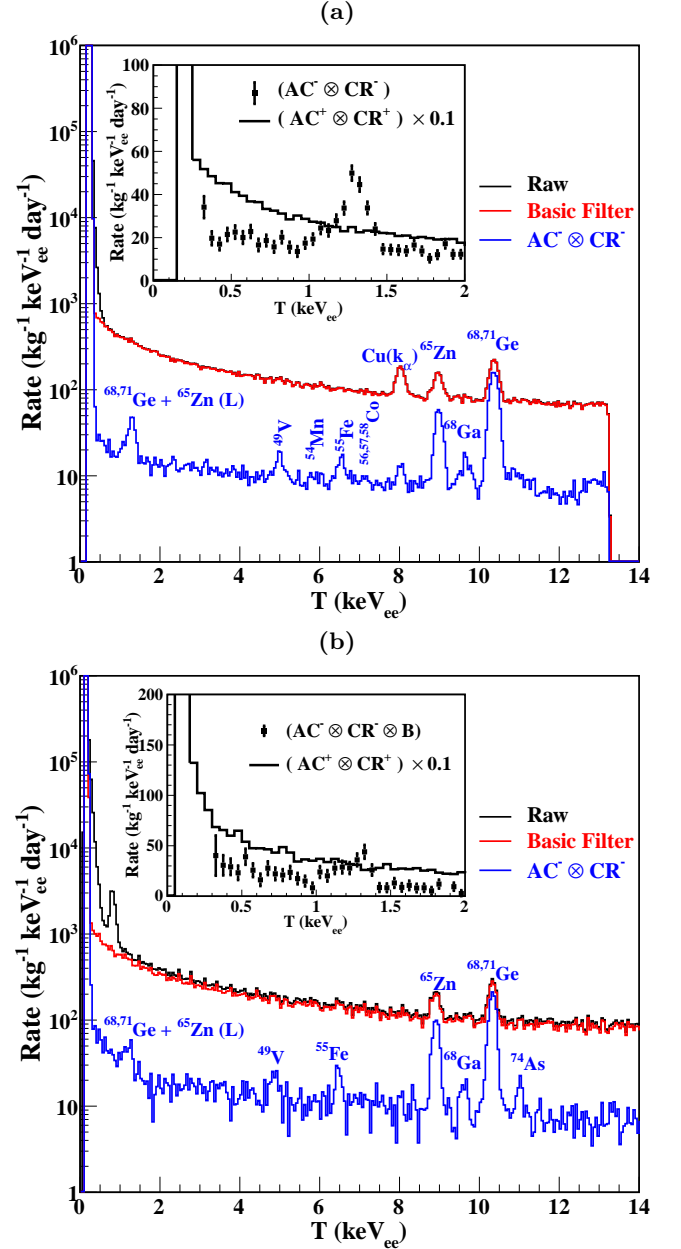


FIG. 18: Evolution of  $\text{AC}^- \otimes \text{CR}^-$  spectra taken with (a) nPCGe and (b) pPCGe at KSNL, from RAW via basic filters of Figures 14a,b&c, AC and CR vetos, and the BS-selection for pPCGe. The triple-coincident  $\text{AC}^+ \otimes \text{CR}^+$  samples are superimposed in the insets, demonstrating that physics events can be probed to a threshold below the electronic noise-edge.

Signal events originated at different parts of the detector fiducial volume exhibit the same pulse shapes for both TA and SA<sub>6</sub>. This feature can be verified by comparing events of different known origins. Events due to external  $\gamma$ -radioactivity are located at shallow depth. For instance,  $\gamma$ -rays of 60 keV and 662 keV from  $^{241}\text{Am}$  and  $^{137}\text{Cs}$  sources would deposit energy in Ge mostly at depth characterized by the attenuation length of 0.96 mm and 27 mm,

TABLE III: Summary table of signal selection procedures in Ge detectors. The pulse maxima ( $A_{max}$ ) is adopted as energy estimator. Low-background data taken at KSNL are used.

Signal Selection	CoaxGe	ULEGe	pPCGe	nPCGe	Uncertainties (%) <sup>II</sup>
1) Trigger					
Pedestal Profile RMS $\sigma_A$ (eV <sub>ee</sub> )	812	33	41	49	2.6
Selected Trigger Level $\Delta$ ( $\sigma_A$ )	4.3	4.3	4.2	4.2	—
Trigger Threshold at $\varepsilon_{\text{Trig}} = 50\%$ (eV <sub>ee</sub> )	3500	142	171	204	1.4
2) DAQ					
$\varepsilon_{\text{DAQ}}$ (%)	N/A *	N/A *	86	87	< 0.1
3) Analysis Selection					
a) Other Detector Systems					
i) $\varepsilon_{\text{CR}}$ of Cosmic-Ray Vetos —		Typical Range	92.1 ± 0.02	%	
ii) $\varepsilon_{\text{AC}}$ of Anti-Compton NaI(Tl) —		Typical Range	99.5 ± 0.06	%	
b) $\epsilon$ of Basic Filters at Noise-Edge (%)					
i) $\Delta t^+ - \Delta t^-$ (Figure 14a)	N/A †	N/A †	97.9	N/A †	< 0.1
ii) Pedestal Range (Figure 14b)	N/A †	N/A †	99.7	99.8	< 0.1
iii) Pulse Maximal Position (Figure 14c)	N/A †	N/A †	99.97	99.98	< 0.1
4) Physics Events Threshold (eV <sub>ee</sub> )					
a) AC <sup>−</sup> ⊗CR <sup>−</sup>	5600	230	311	373	1.3
b) AC <sup>−</sup> ⊗CR <sup>−</sup> ⊗Bulk	N/A †	—	311	—	2.8
c) AC <sup>+</sup> ⊗CR <sup>+</sup>	N/A †	N/A †	197	237	2.3

<sup>II</sup> Uncertainties of pPCGe measurements are quoted as illustration. Other detectors have similar levels.

\* DAQ were shared with a different measurement [9], such that the efficiencies are not relevant to this discussion.

† Hardware configurations and analysis procedures are different in these early measurements.

respectively. On the other hand, events due to internal radioactivity, like X-rays at 10.37 keV<sub>ee</sub> from <sup>68,71</sup>Ge K-shell electron capture to become Ga, are uniformly distributed in the bulk fiducial volume. TA  $\tau$ -distributions of nPCGe and pPCGe for these events are displayed in Figures 17a&b, respectively. Events with AC<sup>+</sup>⊗CR<sup>+</sup> tags, useful for *in situ* calibration purpose, are also included.

The Bulk-to-Surface event ratios of various sources are different in pPCGe, verifying the expectation that these events have different spatial distributions in the detectors. On the other hand, TA  $\tau$ -distributions of Bulk samples are identical among the different samples, demonstrating that detector response is uniform over the entire fiducial volume. Accordingly, it is justified to adopt *in situ* physics background events with AC<sup>+</sup>⊗CR<sup>+</sup> (plus “Bulk” tag for pPCGe) to derive the efficiencies of neutrino- and WIMP-induced signals in AC<sup>−</sup>⊗CR<sup>−</sup> samples, where the feature of single-site events uniformly distributed within the detector volume is identical to that of the internal Ga X-rays.

### (iii) Background Understanding

An interesting note is that AC<sup>+</sup>⊗CR<sup>+</sup> samples of pPCGe shown in Figure 17b have their B-to-S ratio and  $\tau$ -distributions of S-events similar to those of <sup>137</sup>Cs but not <sup>241</sup>Am. This observation indicates that the AC<sup>+</sup>⊗CR<sup>+</sup> events at this specified

energy range (8–12 keV<sub>ee</sub>) are mostly due to external  $\gamma$ -rays of MeV-range energy (rather than 10-keV range) induced by cosmic-rays traversing in the vicinity of the detector. It follows that the studies on timing profiles of S-background events may reveal their origins. This is one of the subjects of our on-going research.

### 3. Combined Background Spectra

Data were taken with various Ge detectors at KSNL. Background events are identified and suppressed when they are (i) correlated with the AC and/or CR systems, (ii) induced by electronic noise with anomalous timing structures, or (iii) located at the surface of pPCGe. The various efficiency factors discussed in this article, namely  $\varepsilon_{\text{Trig}}$ ,  $\varepsilon_{\text{DAQ}}$ ,  $\varepsilon_{\text{CR}}$ ,  $\varepsilon_{\text{AC}}$ ,  $\varepsilon_{\text{bf}}$ ,  $\varepsilon_{\text{BS}}$  and  $\lambda_{\text{BS}}$ , and their uncertainties are applied. Their typical values are summarized in Table III and stated in the respective figures. The combined efficiency for nPCGe is 91% above its noise-edge of 373 eV<sub>ee</sub>, while that for pPCGe is depicted in Figure 13, showing the values before and after BS-selection.

The electronic noise-edge defines the lower reach of the extraction of physics signals for AC<sup>−</sup>⊗CR<sup>−</sup> events which are uncorrelated with other detector systems. The background level at threshold is of  $\mathcal{O}(10 \text{ kg}^{-1} \text{keV}_{\text{ee}}^{-1} \text{day}^{-1})$  at KSNL. The evolution of the energy spectra from raw data via various selection procedures is displayed in Figures 18a&b for nPCGe and pPCGe with 54.6 kg-days and



46.2 kg-days of data, respectively. X-ray lines from internal radioactivity become visible after these selections, and are adopted for energy calibration.

The electronic noise-edge of  $AC^- \otimes CR^-$  events in pPCGe is 311 eV<sub>ee</sub>, as shown in Figures 7b&18b. This threshold applies also to the spectra following the subsequent BS-cut and  $(\varepsilon_{BS}, \lambda_{BS})$ -correction.

As a quantitative illustration, the BS-correction applied to the threshold bin of 300-350 eV<sub>ee</sub> would modify a raw rate of  $B = 98 \pm 20$  in  $\text{kg}^{-1}\text{keV}_{ee}^{-1}\text{day}^{-1}$  unit. The efficiency factors  $(\varepsilon_{BS}, \lambda_{BS}) = (0.80 \pm 0.07, 0.64 \pm 0.01)$  contribute a boost factor of  $[1/(\varepsilon_{BS} + \lambda_{BS} - 1)] = 2.25$  to the statistical uncertainty, giving a corrected value of  $B_0 = 36 \pm 17$ . The systematic uncertainty is  $\pm 19$ , estimated by variations of parameter choice in the derivation of  $(\varepsilon_{BS}, \lambda_{BS})$  [3].

The anomalous surface effects in nPCGe are negligible, so that corrections with  $(\varepsilon_{BS}, \lambda_{BS})$  are not applicable. Physics events can be extracted down to the noise-edge of 373 eV<sub>ee</sub>, as shown in Figures 7c&18a. The noise-edges in both cases, as indicated in Figures 8b&c, are above the range where pulser events exhibit non-linear and anomalous response.

The  $AC^+ \otimes CR^+$  spectra for nPCGe and pPCGe are depicted in the insets of Figures 18a&b, respectively. The triple coincidence of Ge with the AC and CR detector systems with  $AC^+ \otimes CR^+$  tags allow physics signals to be extracted to below the electronic noise-edge defined by anti-coincident  $AC^- \otimes CR^-$  samples. These events can serve as reference samples for efficiency measurements of neutrino- and WIMP-induced events. The energy threshold values are reduced from 373 eV<sub>ee</sub> to 237 eV<sub>ee</sub> and from 311 eV<sub>ee</sub> to 197 eV<sub>ee</sub> for nPCGe and pPCGe, respectively. Below these energies and above the trigger level, electronic self-trigger noise events still overwhelm, despite having coincidence tags with two detector systems.

## V. SUMMARY AND PROSPECTS

Germanium detectors with sub-keV sensitivities have opened windows for studies on SM and exotic neutrino

interactions as well as for searches of light WIMPs. This article documents our efforts on the characterization and optimization of the detector response in energy domains near electronic noise-edge, where the signal amplitude is comparable to that of pedestal fluctuations.

Both pPCGe and nPCGe represent novel advances in Ge detector techniques to measure events with sub-keV energy depositions, and the results of Figures 18a&b and Table III represent improved performance among this class of detectors over those from previous efforts listed in Table II, lowering the detector threshold values from  $\sim 500$  eV<sub>ee</sub> to  $\sim 300$  eV<sub>ee</sub>.

The potential scientific reach depends on the achievable detector threshold. Ongoing R&D efforts are pursued with this goal, via optimizations of hardware configurations, JFET and ASIC electronic components, as well as software pulse-shape discrimination techniques below electronic noise-edge. We note in particular the novel idea of internal amplification in Ge ionization detectors [34].

A new development is the demonstration of the “bolometric amplification” concept in the CDMSlite experiment [35] with Ge crystals operating at cryogenic temperatures. Research programs are pursued to perfect the technique which offers the potential of bringing detector threshold to  $\mathcal{O}(10 \text{ eV}_{ee})$ . Higher cost and technical complications associated with operation at sub-Kelvin temperatures, however, may limit its range of applications.

## VI. ACKNOWLEDGMENTS

This work is supported by the Academia Sinica Investigator Award 2011-15, contracts 99-2112-M-001-017-MY3, 102-2112-M-001-018, 103-2112-M-001-024 and 104-2112-M-001-038-MY3 from the Ministry of Science and Technology, Taiwan. HTW is grateful for a grant from the Simons Foundation and for the hospitality of the Aspen Center for Physics, where part of the manuscript was composed. The authors are grateful to the efforts of Ms. J. Wu and Prof. N. Akchurin on text editing and proof-reading.

- 
- [1] Q. Yue et al., High Energy Phys. and Nucl. Phys. **28**, 877 (2004); H.T. Wong et al., J. Phys. Conf. Ser. **39**, 266 (2006); H.T. Wong, Int. J. Mod. Phys. **D 20**, 1463 (2011).
  - [2] P.S. Barbeau, J.I. Collar, and O. Tench, J. Cosmo. Astropart. Phys. **B 09**, 009 (2007); C.E. Aalseth et al., Phys. Rev. Lett. **101**, 251301 (2008).
  - [3] H.B. Li et al., Astropart. Phys., **56**, 1 (2014).
  - [4] C. Chasman et al., Phys. Rev. Lett. **21**, 20 (1968); K.W. Jones and H.W. Kraner, Phys. Rev. **C 1**, 125 (1971); K.W. Jones and H.W. Kraner, Phys. Rev. **A 11**, 1347 (1975); T. Shutt et al., Phys. Rev. Lett. **69**, 3425 (1992); Y. Messous et al., Astropart. Phys. **3**, 361 (1995); A.R. Sattler et al., Phys. Rev. **143**, 2 (1966); L. Baudis et al., Nucl. Instrum. Meth. **A 418**, 348 (1998); E. Simon et al., Nucl. Instrum. Meth. **A 507**, 643 (2003); A. Benoit et al., Nucl. Instrum. Meth. **A 577**, 558 (2007).
  - [5] C. Giunti and A. Studenikin, Rev. Mod. Phys. **87**, 531 (2015), and references therein.
  - [6] H.T. Wong and H.B. Li, Mod. Phys. Lett. **A 20**, 1103 (2005), and references therein.
  - [7] H.B. Li et al., Phys. Rev. Lett. **90**, 131802 (2003); H.T. Wong et al., Phys. Rev. **D 75**, 012001 (2007).
  - [8] S. Davidson, M. Gorbahn, and A. Santamaria, Phys.

- Lett. **B 626**, 151 (2005); N.F. Bell et al., Phys. Rev. Lett. **95**, 151802 (2005); N.F. Bell et al., Phys. Lett. **B 642**, 377 (2006).
- [9] M. Deniz et al., Phys. Rev. **D 81**, 072001 (2010).
- [10] V.I. Kopeikin et al., Phys. Atom. Nucl. **60**, 2032 (1997); S.A. Fayans, L.A. Mikaelyan and V.V. Sinev, Phys. Atom. Nucl. **64**, 1475 (2001); K.A. Kouzakov, A.I. Studenikin, and M.B. Voloshin, Phys. Rev. **D 83** 113001 (2011); J.W. Chen et al., Phys. Lett. **731**, 159 (2014).
- [11] J.W. Chen et al., Phys. Rev. **D 91**, 013005 (2015).
- [12] J.W. Chen et al., Phys. Rev. **D 90**, 011301(R) (2014).
- [13] A.G. Beda et al., Phys. Part. Nucl. Lett. **10**, 139 (2013).
- [14] J.W. Chen et al., Phys. Rev. **D 93**, 093012 (2016).
- [15] D.Z. Freedman, Phys. Rev. **D 9**, 1389 (1974); D.Z. Freedman, D.N. Schramm, and D.L. Tubbs. Ann. Rev. Nucl. Part. Sci. **27**, 167 (1977); D.K. Papoulias and T.S. Kosmas, Adv. High Energy Phys. **2015**, 763648 (2015).
- [16] D. Akimov, arXiv:1310.0125 (2013), and references therein for current experimental projects.
- [17] S. Kerman et al., Phys. Rev. **D 93**, 113006 (2016).
- [18] M. Drees and G. Gerbier, Review of Particle Physics Chin. Phys. **C 38**, 353 (2014), and references therein.
- [19] H.T. Wong, Mod. Phys. Lett. **A 23**, 1431 (2008); S.T. Lin et al., Phys. Rev. **D 79**, 061101(R) (2009).
- [20] H.B. Li et al., Phys. Rev. Lett. **110**, 261301 (2013).
- [21] C.E. Aalseth et al., Phys. Rev. Lett. **106**, 131301 (2011); C.E. Aalseth et al., Phys. Rev. Lett. **107**, 141301 (2011); C.E. Aalseth et al., Phys. Rev. **D 88**, 012002 (2013); C.E. Aalseth et al., arXiv:1401.3295 (2014).
- [22] S.K. Liu, Phys. Rev. **D 90**, 032003 (2014).
- [23] K.J. Kang et al., Chin. Phys. **C 37**, 126002 (2013); W. Zhao et al., Phys. Rev. **D 88**, 052004 (2013); Q. Yue et al., Phys. Rev. **D 90**, 091701(R) (2014); W. Zhao et al., Phys. Rev. **D 93**, 092003 (2016).
- [24] G.K. Giovanetti et al., Phys. Procedia **00**, 1 (2014).
- [25] P.N. Luke et al., IEEE Trans. Nucl. Sci. **B 36**, 926 (1989).
- [26] A. Morales et.al, Phys. Lett. **B 489**, 268 (2000).
- [27] S. Riboldi et al., Proc. IEEE-NSS/MIC, 1 (2013); N. Abgrall, et al., Adv. High Energy Phys. **2014**, 365432 (2014); G. Benato et al., Phys. Procedia **61**, 673 (2015).
- [28] E. Aguayo et al., Nucl. Instrum. Meth. **A 701**, 176 (2013); H. Jiang et al., Chin. Phys. **C 40**, 096001 (2016).
- [29] F. Ziegler, Transport of Ions in Matter, <http://www.srim.org> (1998).
- [30] J. Lindhard et al., Mat. Fys. Medd. K. Dan. Vidensk. Selsk. **B 33**, 10 (1963).
- [31] U. Tamm, W. Michaelis, and P. Coussieu, Nucl. Instrum. Meth. **48**, 301 (1967); M.G. Strauss and R.N. Larsen, Nucl. Instrum. Meth. **56**, 80 (1967); E. Sakai, IEEE Trans. Nucl. Sci. **18**, 208 (1971).
- [32] J. Bendat, in *Principles and Applications of Random Noise Theory* Pg. 127, Wiley and Son, (1958); P.J. Statham, X-ray Spect. **6**, 94 (1977).
- [33] M. Agostini et al., Eur. Phys. J. **C 73**, 2583 (2013).
- [34] A.S. Starostin and A.G. Beda, Phys. Atom. Nucl. **63**, 1297 (2000).
- [35] B. Neganov and V. Trofimov, Otkrytiya, Izobret. **146**, 215 (1985); P. Luke et al., Nucl. Instrum. Meth. **A 289**, 406 (1990); R. Agnese et al., Phys. Rev. Lett. **112**, 041302 (2014); R. Agnese et al., Phys. Rev. Lett. **116**, 071301 (2016).